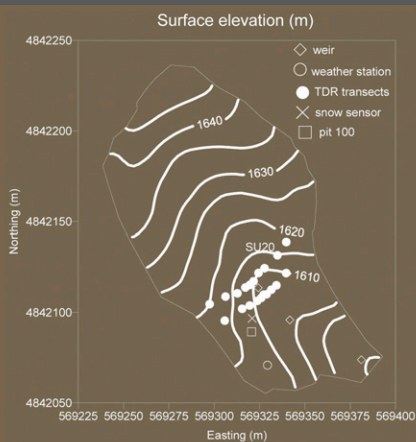


T. J. Kelleners*
D. G. Chandler
J. P. McNamara
M. M. Gribb
M. S. Seyfried



A new distributed model was developed for calculating vertical and lateral water and heat exchange in complex terrain. Model results for a small catchment near Boise, ID, showed that 11 to 16% of incoming yearly precipitation is transformed into streamflow, compared with measured values that ranged between 14 and 34%.

T.J. Kelleners, Renewable Resources Dep., Univ. of Wyoming, Laramie, WY 82071; D.G. Chandler, Dep. of Civil Engineering, Kansas State Univ., Manhattan, KS 66506; J.P. McNamara, Dep. of Geosciences, Boise State Univ., Boise, ID 83725; M.M. Gribb, Dep. of Civil Engineering, Boise State Univ. Boise, ID 83725; and M.S. Seyfried, USDA-ARS Northwest Watershed Research Center, Boise, ID 83712. *Corresponding author (tkellene@uwyo.edu).

Vadose Zone J. 9:517–527
doi:10.2136/vzj2009.0033
Received 31 Mar. 2009.
Published online 11 Jan. 2010.

© Soil Science Society of America
5585 Guilford Rd., Madison, WI 53711 USA.
All rights reserved. No part of this periodical may be reproduced or transmitted in any form or by any means, electronic or mechanical, including photocopying, recording, or any information storage and retrieval system, without permission in writing from the publisher.

Modeling Runoff Generation in a Small Snow-Dominated Mountainous Catchment

Snowmelt in mountainous areas is an important contributor to river water flows in the western United States. We developed a distributed model that calculates solar radiation, canopy energy balance, surface energy balance, snow pack dynamics, soil water flow, snow–soil–bedrock heat exchange, soil water freezing, and lateral surface and subsurface water flow. The model was applied to describe runoff generation in a subcatchment of the Dry Creek Experimental Watershed near Boise, ID. Calibration was achieved by optimizing the soil water field capacity (a trigger for lateral subsurface flow), lateral saturated soil hydraulic conductivity, and vertical saturated hydraulic conductivity of the bedrock. Validation results show that the model can successfully calculate snow dynamics, soil water content, and soil temperature. Modeled streamflow for the validation period was underestimated by 53%. The timing of the streamflow was captured reasonably well (modeling efficiency was 0.48 for the validation period). The model calculations suggest that 50 to 53% of the yearly incoming precipitation in the subcatchment is consumed by evapotranspiration. The model results further suggest that 34 to 36% of the incoming precipitation is transformed into deep percolation into the bedrock, while only 11 to 16% is transformed into streamflow.

Abbreviations: EF, modeling efficiency; LAI, leaf area index; SWE, snow water equivalent; TDR, time domain reflectometry.

Runoff due to snowmelt from mountainous catchments is an important source of water in the western United States. It may also pose a hazard, as localized spring flooding is not uncommon. The quantity and timing of the runoff depend on a large number of interacting factors. These factors are related to climate, topography, subsurface morphology, and vegetation. Recent studies have highlighted the fact that watershed soils need to cross a certain wetness threshold before water inputs due to rainfall or snowmelt generate streamflow (Buttle et al., 2004; Tromp-van Meerveld and McDonnell, 2006). Exceeding this threshold causes the watershed to become laterally connected, allowing rapid water flow from the watershed to the stream (Seyfried et al., 2009). The threshold behavior may be particularly important in semiarid areas that undergo large fluctuations in soil water storage during the year (McNamara et al., 2005).

Direct measurement of the variables that are involved in runoff generation is usually limited to only a few locations. Hydrologic models can provide the framework for analyzing the runoff processes in more detail (Singh and Frevert, 2002). Parameterization of watershed models has traditionally been problematic due to the large number of parameters involved and due to the spatial variability in many of these parameters; however, recent developments in sensor technology and parameter optimization have considerably improved our ability to calibrate hydrologic models (Vrugt et al., 2003; Robinson et al., 2008).

Hydrologic models have been used to study runoff generation from individual hillslopes, small catchments, and complete river basins. Distributed modeling approaches have become popular as computing power has increased because these models quantify the processes in a spatially explicit manner (Beven, 1989; Ivanov et al., 2004). The detail of the modeled processes generally decreases as the spatial scale for which the model is intended increases. A comprehensive overview of existing distributed hydrologic models can be found in Kampf and Burges (2007).

Interception of precipitation by plant canopies and root water uptake can have an important impact on soil moisture status and hence runoff generation. The effect of vegetation on the surface energy balance and on the soil water balance is usually represented in a simplified manner in hydrologic models. Examples of hydrologic models with a relatively detailed vegetation parameterization can be found in Wigmosta et al. (1994, 2002) and Kavvas et al. (1998, 2004). Land surface models developed by the climate science community generally have more elaborate vegetation parameterizations but lack the ability to calculate lateral surface and subsurface water flow (Dickinson et al., 1993; Bonan, 1996; Oleson et al., 2004).

Snow accumulation and snowmelt also have a significant impact on the surface energy balance and the soil water balance, especially in snow-dominated systems. Many hydrologic models treat snow in a simplified manner. The snowpack is represented by a single layer (Downer and Ogden, 2004), two layers (Wigmosta et al., 2002), or three layers (Kavvas et al., 2004). In reality, snow is made up of multiple layers, with each layer having its own thickness, snow grain size, density, water content, and energy content. Specialized snow physical algorithms as developed by Anderson (1976), Jordan (1991), and Dai and Zeng (1997) facilitate a more realistic parameterization of snow (Oleson et al., 2004). Soil water freezing, which may be important during cold periods with thin or nonexistent snowpack, is generally ignored in distributed hydrologic models.

For this study, we developed a distributed hydrologic model by combining an algorithm for one-dimensional vertical water flow and heat transport developed by Kelleners et al. (2009) with relatively simple lateral surface and subsurface water flow routines. The one-dimensional model provides a detailed description of the water and energy fluxes through vegetation, snow, soil, and bedrock for each grid cell in the distributed model. We hypothesize that a detailed physical representation of vegetation and snow is important to describe runoff generation in snow-dominated mountainous terrain. The model is a considerable departure from most existing hydrologic models where the main emphasis is on the lateral water flow processes instead of on the vertical water and heat exchange processes (e.g., Kampf and Burges, 2007). The specific objectives of the study were to: (i) develop a computer model that describes vertical water and heat exchange as well as lateral surface and subsurface water flow in snow-dominated mountainous catchments; and (ii) apply the model to a small mountainous catchment to quantify runoff generation in a snow-dominated system.

Model Description

Digital elevation data are used to divide the catchment into grid cells of 10 by 10 m and to determine the slope, aspect, and surface area of each cell. The 10-m grid size is a good compromise between spatial resolution and data volume for hydrologic simulations in areas with moderate to steep slopes (Zhang and Montgomery, 1994). The soil

and the underlying bedrock within each cell are discretized vertically to facilitate the numerical solution of vertical water flow and heat transport equations. Lateral surface and subsurface flow are incorporated in a simplified manner using sink–source terms in the vertical soil water flow equations. The sink–source terms are calculated using water potentials from the previous time step. Streamflow is not calculated explicitly. Instead, surface ponding at the catchment outlet due to incoming surface runoff and saturation of the outlet grid cell is simply removed from the model and classified as streamflow. The outer boundary of the flow domain is treated as a no-flow boundary. This implies that hyporheic flow is not considered at the outlet.

Vegetation is characterized by specifying vegetation height, leaf area index, stem area index, and soil cover. Stomatal conductance is calculated as a function of net incoming visible solar radiation and soil water pressure head. A uniform rooting system is assumed that covers the entire soil depth. Snow accumulation is accounted for by using a multilayer algorithm based on the work of Jordan (1991). Thickness, density, and grain diameter are calculated as a function of time for all individual snow layers. For each grid cell, separate energy balance calculations are conducted for the vegetation and the ground surface (soil or snow) by solving for leaf temperature and ground surface temperature. Ground albedos for soil without snow are calculated from the soil color class, topsoil water content, and wavelength. Ground albedos for snow-covered surfaces are determined by snow soot content, snow grain radius, wavelength, and illumination angle.

Meteorological input data such as precipitation, temperature, relative humidity, wind speed, and cloudiness are the main model drivers. Time stepping is 15 min except for the soil water flow calculations, which may use smaller time steps. Details on the parameterization for stand-alone grid cells are given in Kelleners et al. (2009), who calculated vertical water and energy exchange for a single point in the landscape. In this study, we focused primarily on the lateral water and energy exchange components that were combined with the point model to obtain a distributed model that can calculate water and energy exchange in complex terrain.

Surface Energy Balance in Complex Terrain

To calculate the vegetation and ground surface energy balance for each grid cell in complex terrain, we modified the calculations for short- and longwave radiation. The blocking of direct incoming solar radiation by the surrounding terrain is incorporated in the catchment model using the algorithm of Dozier and Outcalt (1979). First, a set of horizon angles are generated by calculating the vertical angle from the specified point to every other point in the grid whose elevation is greater. Next, the terrain that surrounds each grid cell is divided into sectors and a maximum horizon angle is identified for each sector. These calculations are conducted only once at the start of each model run. Subsequently, the appropriate sector for each time step is selected based on a comparison with the current solar azimuth angle. Finally, direct incoming solar radiation to a particular grid cell is considered

blocked when the solar altitude angle is smaller than the maximum horizon angle for that cell, given the selected sector.

Incoming direct and diffuse solar radiation due to reflection from the surrounding terrain (I_{dirr} and I_{difr} , respectively) are estimated as

$$I_{\text{dirr}}(\lambda) = I_{\text{dir}}(\lambda) \bar{\alpha}_{\text{g}}^{\mu}(\lambda)(1-V) \quad [1a]$$

$$I_{\text{difr}}(\lambda) = I_{\text{dif}}(\lambda) \bar{\alpha}_{\text{g}}(\lambda)(1-V) \quad [1b]$$

where I_{dir} and I_{dif} are the direct and diffuse radiation on a horizontal surface, $\bar{\alpha}_{\text{g}}^{\mu}$ and $\bar{\alpha}_{\text{g}}$ are the catchment-average ground albedos for direct (superscript μ) and diffuse radiation, λ is the wavelength, and V is the view factor, calculated as

$$V = \cos^2 \left(\frac{\sum \beta}{n_s} \right) \quad [2]$$

where β is the maximum horizon angle of a particular sector and n_s is the number of sectors for each grid cell. The view factor can be interpreted as the fraction of open sky seen by the grid cell, i.e., that part of the horizon that is not blocked by the surrounding terrain (Muneer, 1997). This factor is also used to reduce the amount of incoming diffuse solar radiation and incoming longwave radiation from the sky for grid cells that are surrounded by higher ground. Finally, the relative contributions of the sky and the surrounding terrain to net longwave radiation at the ground surface, L_{ng} , are approximated using (Marks and Dozier, 1979)

$$L_{\text{ng}} = \beta_{\text{g}} \varepsilon_{\text{a}} \sigma T_{\text{a}}^4 \min(\cos^2 i/2, V) + (1-V) \beta_{\text{g}} \varepsilon_{\text{g}} \sigma T_{\text{g}}^4 - \varepsilon_{\text{g}} \sigma T_{\text{g}}^4 \quad [3]$$

where ε is emissivity, β is absorptivity, σ is the Stefan–Boltzmann constant, i is ground surface slope angle, T is absolute temperature, and subscripts a and g stand for air and ground, respectively. In using Eq. [3], we assumed that the surrounding terrain (second term on the right side) has the same temperature as the point under consideration and that vegetation does not interfere with this portion of the incoming longwave radiation. No modifications were made in the sensible and latent heat flux calculations for each grid cell as presented in Kelleners et al. (2009).

Water Flow

Vertical soil water flow for each grid cell is calculated using a non-iterative solution to Richards' equation. The water balance for each vertical element i can be written as (after Ross, 2003)

$$d_i \frac{\Delta \theta_{wi}}{\Delta t} = q_{i+1}^F - q_i^F - S_{\text{root},i}^0 d_i \pm S_{\text{subn},i}^0 d_i \quad [4]$$

$i = 1, \dots, N$

where d is the element thickness, θ_w is the volumetric soil water content, t is time, q is the vertical soil water flux at a fraction F through the time step, S_{root} is a sink term due to root water uptake, S_{subn} is a sink–source term due to net subsurface lateral soil water flow, and N is the number of soil elements (numbering from the bottom up). Both S_{root} and S_{subn} are evaluated at the beginning of the time step (superscript 0). The flux q at fraction F through the time step is estimated using a Taylor series expansion:

$$q_i^F = q_i^0 + F \left(\left. \frac{\partial q_i}{\partial u_i} \right| \Delta u_i + \left. \frac{\partial q_i}{\partial u_{i-1}} \right| \Delta u_{i-1} \right) \quad [5]$$

where u is either θ_w (unsaturated layer) or the soil water pressure head h (saturated layer, where $\Delta \theta_w = 0$). The soil water flux at the beginning of the time step is calculated using the Darcy equation:

$$q_i^0 = \frac{K_i + K_{i-1}}{2} \left(\frac{h_i - h_{i-1}}{\Delta z_i} + 1 \right) \quad [6]$$

where K is the soil hydraulic conductivity and z is the vertical coordinate. The derivatives of the soil water flux at the beginning of the time step in Eq. [5] can be obtained by differentiating the Darcy equation with respect to either θ_w or h . An additional balance equation for pond height, h_0 , is included if ponding occurs on the soil surface (after Ross, 2003):

$$\frac{\Delta h_0}{\Delta t} = q_{\text{top}}^F - q_{\text{surf}}^F \pm S_{\text{surfn}}^0 h_0 \quad [7]$$

where q_{top} is the net incoming water flux from precipitation and surface evaporation (no snow) or snowmelt, q_{surf} is the vertical flux at the soil surface, and S_{surfn} is the sink–source term due to net incoming and outgoing surface runoff. The surface flux is again estimated using a Taylor series expansion:

$$q_{\text{surf}}^F = q_{\text{surf}}^0 + F \left(\left. \frac{\partial q_{\text{surf}}}{\partial h_0} \right| \Delta h_0 + \left. \frac{\partial q_{\text{surf}}}{\partial u_N} \right| \Delta u_N \right) \quad [8]$$

The surface flux at the beginning of the time step is

$$q_{\text{surf}}^0 = K_N \left(\frac{h_0 - h_N}{0.5d_N} + 1 \right) \quad [9]$$

Incoming surface runoff into a grid cell without a ponding layer is accommodated by incorporating S_{surfn} into the water balance equation for the top soil element. The sink terms S_{surf} and S_{sub} that are used to calculate the net lateral surface and subsurface fluxes for each individual grid cell are given by

$$S_{\text{surfn},j} = \frac{f_{1j} Q_{\text{surf}}}{\sum f_{1j} A b_0} \quad j = 1, \dots, 8 \quad [10a]$$

$$S_{\text{sub},i,j} = \frac{f_{1j}f_{2i}}{\sum f_{1j} \sum f_{2i}} \frac{Q_{\text{sub}}}{Ad_i} \quad i = 1, \dots, N \quad j = 1, \dots, 8 \quad [10b]$$

where f_1 is the fraction of surface runoff or subsurface lateral flow that moves to the j th neighboring grid cell, f_2 is the fractional contribution of the i th soil layer to subsurface lateral flow, Q_{surf} is the surface runoff for the cell under consideration, Q_{sub} is the subsurface lateral flow for the cell under consideration, and A is the area of the grid cell. Only saturated soil layers generate and receive lateral subsurface flow in the model. These saturated layers are identified from the bottom up so that isolated saturated soil layers near the surface are not involved in the lateral exchange. The first unsaturated soil layer from the bottom with $\theta_{fc} < \theta_w + \theta_i < \phi$ is considered partially saturated, where θ_{fc} is the field capacity, θ_i is the ice content, and ϕ is the porosity. The contribution ΔH to the total saturated height H of this single partially saturated layer is calculated as

$$\Delta H = d_i \frac{\theta_{wi} + \theta_{ii} - \theta_{fc}}{\phi - \theta_{fc}} \quad \theta_{wi} + \theta_{ii} > \theta_{fc} \quad [11]$$

All incoming lateral subsurface flow is directed to the bottom soil layer of a grid cell if no saturated layer exists. The concept of a single partially saturated layer possibly contributing to lateral subsurface flow is included to allow lateral flow through unsaturated soil profiles in steep terrain. This type of lateral flow can be switched off by setting θ_{fc} equal to ϕ . The fractions f_1 are determined by dividing the water level elevation differences between the current grid cell

and its neighbors by the respective horizontal distances. As a result, most of the lateral flow will move in the direction of the steep descent. The water level elevation for surface ponding water is the sum of the soil surface elevation and the ponding depth. The water level elevation for saturated soil layers is equal to the soil surface elevation – soil depth + H . The fractions f_2 are calculated by assuming that the contribution of each saturated soil layer to lateral flow is proportional to the ratio of its saturated thickness to H . The surface runoff Q_{surf} is calculated using the Manning equation for overland flow (Hillel, 2004):

$$Q_{\text{surf}} = w \frac{k}{n} h_0^{5/3} \sin^{1/2}(i) \leq \frac{h_0 A}{\Delta t} \quad [12]$$

where w is the grid cell width, k is $1 \text{ m}^{1/3} \text{ s}^{-1}$, and n is the dimensionless roughness coefficient. Lateral subsurface flow Q_{sub} is calculated using the kinematic approximation (Beven, 1981; Kampf and Burges, 2007):

$$Q_{\text{sub}} = w K_s H \sin(i) \leq \frac{H(\phi - \theta_{fc}) A}{\Delta t} \quad [13]$$

where K_s is the lateral saturated soil hydraulic conductivity. The calculated values for Q_{surf} and Q_{sub} are both limited to the amount that is actually available for lateral flow to avoid overdraft.

The soil water flow calculations are initiated by specifying the soil water content and soil ice content as a function of depth for each grid cell. Equations [4] and [7] are solved simultaneously when surface ponding occurs (for details, see Ross, 2003; Kelleners et al., 2009). The upper boundary is always described by a flux condition. This flux is determined by the difference between rainfall and evaporation (no snow) or by the melt flux from the bottom snow layer. The bottom boundary is ill defined in most mountainous terrain due to uncertainty about the exact flow conditions at the soil–bedrock interface. Downward percolation flux, q_{dp} , into the bedrock is calculated using the following approximation:

$$q_{dp} = \begin{cases} K_{sr} \frac{H+D}{D} & H > 0 \\ 0 & H = 0 \end{cases} \quad [14]$$

where K_{sr} is the vertical saturated hydraulic conductivity of the bedrock and D is the thickness of the upper portion of the bedrock that is assumed saturated during deep percolation events. Both K_{sr} and D are essentially unknowns. In this study, we fixed D to 0.2 m and treated K_{sr} as a fitting parameter. No detailed bedrock water flow is calculated by the model and downward percolation across the soil–bedrock interface is simply removed from the model and classified as deep percolation. The above equations result in a tri-diagonal system of equations for each grid cell that is solved using the Thomas algorithm (Press et al., 1992). No iteration between grid cells is required because all lateral water fluxes are known at the start of the time step.

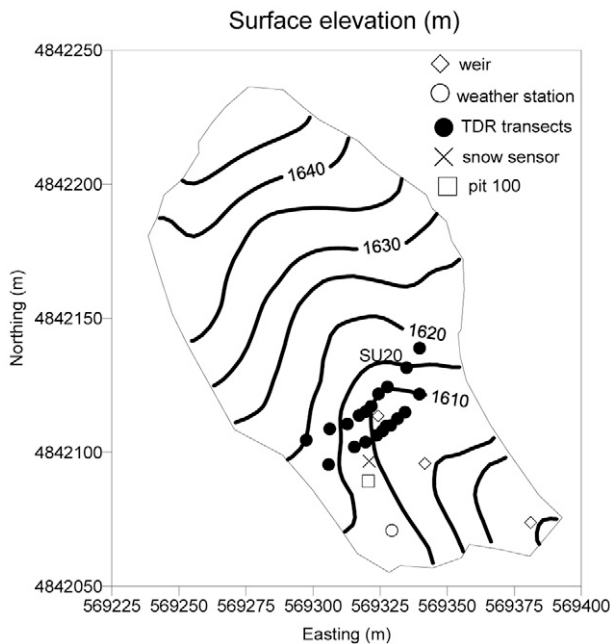


Fig. 1. Surface elevation contours and instrumentation locations for the 0.0141-km² subcatchment of the Dry Creek Experimental Watershed near Boise, ID.

Heat Transport

Vertical heat transport in the snow–soil–bedrock continuum is described using the following general equation for heat conduction and advection:

$$\frac{\partial(C_v T)}{\partial t} = \frac{\partial}{\partial z} \left(\kappa \frac{\partial T}{\partial z} \right) + C_{v,w} \frac{\partial(qT)}{\partial z} - C_{v,w} S_{\text{root}} T \quad [15]$$

where C_v is the volumetric heat capacity, T is the temperature, and κ is the thermal conductivity. The subscript w denotes liquid water. The possible presence of ponded water on the soil surface is ignored in the vertical heat transport calculation. Also, no lateral heat transport is calculated. The effect of these simplifications on the calculated heat transport is limited because the surface pond height is generally small and because most lateral heat transport takes place during the snowmelt season when water is close to 0°C, advecting little heat. Heat transport is initialized by specifying snow, soil, and bedrock temperatures. The top boundary is either the snow surface or the soil surface and is described by a heat flux condition as determined by the surface energy balance. The bottom boundary for heat transport is specified at some depth in the bedrock. Here a constant temperature is prescribed, representing the annual average air temperature in the area (e.g., Slagstad et al., 2008). The resulting tri-diagonal system of equations for heat transport in each grid cell is solved using the Thomas algorithm.

Snow and soil water phase change from liquid water to ice is calculated after the soil water flow and heat transport calculations are completed. The liquid water–ice phase change in a snow layer depends on the layer temperature and on the net incoming heat flux. In the soil, the energy state of the liquid water also plays a role. Capillary forces and dissolved ions reduce the energy state of the soil water, resulting in freezing temperatures below 0°C. The procedure is based on the work of Oleson et al. (2004) and is explained in detail in Kelleners et al. (2009). Soil and snow water vapor transport is not included in the model.

Materials and Methods

Study Area

The model was applied to a 0.0141-km² subcatchment of the Dry Creek Experimental Watershed near Boise, ID (Fig. 1). The subcatchment elevation ranges from 1600 to 1645 m above sea level. The summers are hot and dry. Winters are cold, with a persistent snowpack from around early November through March or April. Approximately half of the average annual precipitation of 570 mm falls as snow. Soils typically contain a significant coarse fraction (>2 mm) and classify as gravelly sand, loamy sand, and sandy loam. The soils vary in thickness from a few centimeters to about 1 m and are formed from weathering of the underlying granitic intrusion, called the Idaho Batholith. A network of fractures in the bedrock enables deep percolation when the soil–bedrock interface is wet (Miller et al., 2008). The vegetation consists of sagebrush (*Artemisia tridentata* Nutt.), forbs, and grasses

(Williams, 2005; McNamara et al., 2005). Slopes of up to 60% are found in the subcatchment.

The monitoring program in Dry Creek began in 1999. The subcatchment is equipped with a small meteorological station that measures precipitation, barometric pressure, air temperature, relative humidity, wind speed, wind direction, and incoming solar radiation. Snow depth on the northeast-facing slope is measured hourly using a Judd ultrasonic depth sensor (Judd Communications, Salt Lake City, UT). Soil water content as a function of depth is measured using CS615 water content reflectometers (Campbell Scientific, Logan, UT) and time domain reflectometry (TDR100, Campbell Scientific, Logan, UT). The CS615 sensors are installed in two pits on the northeast-facing slope. The TDR100 waveguides are installed along two parallel transects perpendicular to the ephemeral stream, covering both the northeast- and southwest-facing slopes. Soil temperature as a function of depth is measured using thermocouples in the same two pits that contain the CS615 sensors. Streamflow is measured using three weirs at 10, 50, and 70 m from the outlet of the subcatchment. The stage of the weirs is monitored using pressure transducers. Measured streamflow varies little between weirs and only data of the weir at 10 m from the outlet was used in this study.

The CS615 sensors were calibrated using manual readings from collocated TDR waveguides (Chandler et al., 2004). The TDR sensor readings were converted to soil water content using the relationship of Topp et al. (1980) for high-frequency TDR systems. In this study, we used only data from the CS615 sensors and thermocouples in one pit on the northeast-facing slope. The CS615 sensors in this pit (Pit 100 of McNamara et al., 2005) are installed at 5-, 10-, 30-, 60-, and 100-cm depths. The thermocouples are installed at 5, 15, 30, 60, and 100 cm. The use of TDR transect data was limited to one location on the southwest-facing slope. Waveguides at this location (designated SU20) are installed at 12- and 34-cm depths. A snow survey was conducted on 10 Feb. 2004 covering 57 points across the subcatchment using a snow tube. The resulting snow height and snow water equivalent (SWE) data were used for model validation.

Modeling Setup

The subcatchment was partitioned into 141 grid cells of 10 by 10 m using digital elevation data. Measured soil depths in the subcatchment ranged between 0.21 and 1.25 m (Williams, 2005), resulting in an average soil depth of 0.48 m. Interpolated soil depths for each of the 141 model grid cells were discretized into seven layers of equal thickness. The underlying bedrock was discretized using five layers of equal thickness up to a depth of 10.45 m below the soil surface. The relatively coarse vertical discretization was a compromise between the computational burden and the model's ability to represent realistic subsurface moisture and temperature profiles. The relatively thick subsurface used was important to account for the dampening effect of the bedrock heat storage on the seasonal soil temperature variations. The prescribed constant temperature in the bedrock at 10.45-m depth was 8.5°C.

Two full years were simulated for which a relatively complete data set was available using a basic time step of 15 min. The period of 25 Aug. 2000 to 24 Aug. 2001 served as the calibration period. The period of 20 Aug. 2003 to 19 Aug. 2004 served as the validation period. Both periods started in August because of the relatively well-defined conditions during this month. By the end of August, the growing season is ending, soil water storage is depleted, and soil temperature is near its annual maximum. Also, it is safe to assume that there is no snow accumulation and that the soil ice content is zero. Preparation of the model input data describing the general atmospheric conditions and the meteorological driver variables is discussed in Kelleners et al. (2009). Measured incoming solar radiation was not used directly in the model. Instead, the solar radiation data were used to determine the cloudiness at 15-min intervals. The cloudiness information was then used to calculate the incoming solar radiation for each grid cell individually.

Vegetation in the subcatchment consisted mainly of sagebrush, forbs, and grasses. The presence of a number of scattered trees was ignored in the model. A constant vegetation height of 0.4 m was used. Measured vegetation soil cover (SC_m) in the catchment during the summer growing season varied between 0.05 and 1 (Williams, 2005). The maximum leaf area index LAI_{max} , the

minimum leaf area index LAI_{min} , and the stem area index SAI of a single average plant in the catchment were estimated at 2.3, 0.2, and 0.2, respectively. In principle, bare areas and vegetated areas can be treated separately by the model; however, this is probably not appropriate when the bare and vegetated areas are closely interspersed such as at our catchment. Instead, we chose to consider the entire catchment as vegetated ($SC = 1$), with adjusted LAI_{max} , LAI_{min} , and SAI values for each of the 141 model grid cells of $2.3SC_m$, $0.2SC_m$, and $0.2SC_m$, respectively. The actual LAI for each cell was assumed to be a function of the depth-average soil temperature (Dickinson et al., 1993):

$$LAI = LAI_{min} + (LAI_{max} - LAI_{min}) \left[1 - 0.0016(25 - \bar{T}_{soil})^2 \right] \quad [16]$$

where T_{soil} is the soil temperature ($^{\circ}C$). Plant optical properties and plant aerodynamic parameters used in the vegetation energy balance calculations for each grid cell were represented by parameters for the “broadleaf evergreen shrub–temperate” plant functional type as given by Oleson et al. (2004). Initial soil water content, soil temperature, and bedrock temperature were approximated by running the model twice, first with estimated initial values and then with initial values derived from the final calculated values from the first run.

Model Calibration

During model calibration it was assumed that the soils are horizontally and vertically homogeneous throughout the catchment and that the bedrock parameters K_{sr} and D (Eq. [14]) do not vary in space. The Brooks and Corey (1964) parameters describing the soil hydraulic properties were taken from Kelleners et al. (2009), who calibrated the one-dimensional point model for the north-east-facing slope of the catchment. The current model calibration focused on parameters that describe lateral subsurface water flow and deep percolation. The calibrated parameters are the field capacity θ_{fc} (a trigger for lateral subsurface flow), the lateral saturated soil hydraulic conductivity K_s (Eq. [13]), and the vertical saturated hydraulic conductivity of the bedrock K_{sr} (Eq. [14]). The surface roughness n for overland flow was not calibrated because overland flow is rarely observed on the hillslopes in the catchment. Instead, a constant value of $n = 0.13$ was selected, representative of overland flow across vegetated surfaces (Dingman, 2002). No surface energy balance, vegetation, snow, or subsurface heat transport parameters were calibrated.

The optimum parameter values for θ_{fc} , K_s , and K_{sr} were obtained by inverse modeling of the calibration period using the global parameter optimization software MCS (Huyer and Neumaier, 1999). The objective function for the parameter optimization consisted of streamflow data from the weir at 10 m from the outlet (measured at 15-min intervals) and profile-average soil water content data from Pit 100 on the northeast-facing slope (measured at hourly intervals). The likelihood of finding unique parameter values was

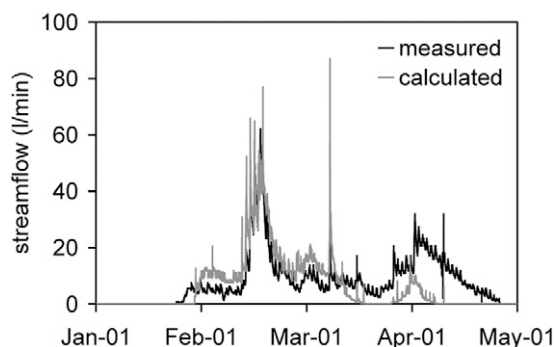


Fig. 2. Measured and calculated streamflow for the weir at 10 m from the outlet of the subcatchment for the calibration period.

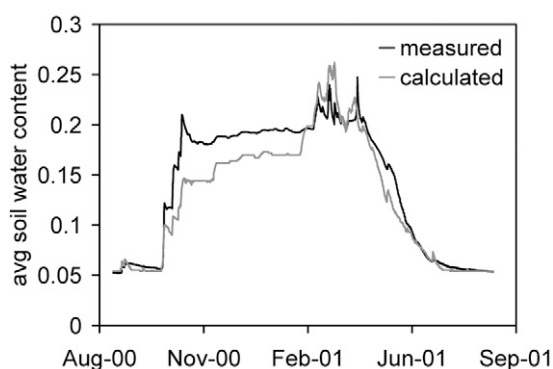


Fig. 3. Measured and calculated profile-average soil water content for Pit 100 on the northeast-facing slope of the subcatchment for the calibration period.

increased by combining different data types in the objective function. The objective function Φ was written as

$$\Phi = v_j \sum (Q_{\text{stream}i}^* - Q_{\text{stream}i})^2 + v_j \sum (\bar{\theta}_i^* - \bar{\theta}_i)^2 \quad [17]$$

where Q_{stream} is the measured (asterisk) and calculated (no asterisk) streamflow, $\bar{\theta}$ is the measured (asterisk) and calculated (no asterisk) profile-average soil water content, and v is a weighting coefficient that accounts for differences in absolute values and number of data points between data types (Clausnitzer and Hopmans, 1995):

$$v_j = 1/N_j \sigma_j^2 \quad [18]$$

where N is the number of data points and σ^2 is the measurement variance. The model calibration and validation were evaluated using graphical comparisons and modeling statistics. Two generally recommended statistical model indicators were used, RMSE and modeling efficiency (EF) (Loague and Green, 1991; Vanclouster et al., 2000; Fernandez et al., 2002). The RMSE statistic gives the percentage of overestimation or underestimation of the predicted value compared with the mean observed value. The EF statistic indicates the degree to which the predictions give a better estimate of the observations than the mean of the observations (Fernandez et al., 2002). The maximum value for EF is 1. If EF is <0, the model-predicted values are worse than simply using the observed mean (Loague and Green, 1991).

Results and Discussion

Model Calibration Results

The measured and calculated streamflow is shown in Fig. 2 (RMSE = 81%, EF = 0.11). The figure shows that the overall dynamics of the system are captured reasonably well by the model. The low EF = 0.11 for the streamflow is disappointing. Close examination of Fig. 2 shows that most of the discrepancies between measured and calculated values occur toward the end of the runoff season in late April. Measured streamflow is still considerable during this period while calculated streamflow has ceased. This discrepancy may be due to input data limitations and model limitations. Input limitations include sparse soil depth data (57 points for 141 grid cells) and sparse soil water retention data (one sample). Model limitations include the assumption of purely Darcian flow, the assumption of a sharp soil–bedrock interface, and the assumption of all deep percolation into the bedrock being lost from the catchment. Interconnected soil macropores may result in rapid soil water flow toward the stream. In addition, part of the water that percolates into the bedrock may still reach the stream, especially if the upper part of the bedrock is weathered. Inaccuracies in the amount and timing of water input from snowmelt may also explain some of the discrepancy between the measured and calculated streamflows. The distinct peak in the calculated streamflow on 25 March is due to a rain-on-snow event.

Table 1. Yearly water balance for the calibration and validation periods for the subcatchment.

Water balance term	Calibration	Validation
	mm	
Precipitation	590	716
Evapotranspiration	311	357
Deep percolation	215	240
Streamflow	64	113
Change in soil water storage	0	6

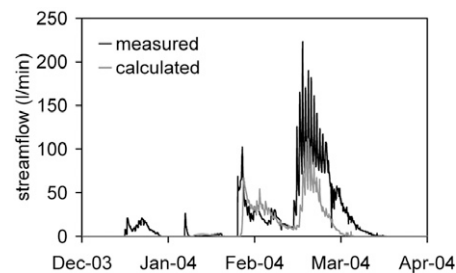


Fig. 4. Measured and calculated streamflow for the weir at 10 m from the outlet of the subcatchment for the validation period.

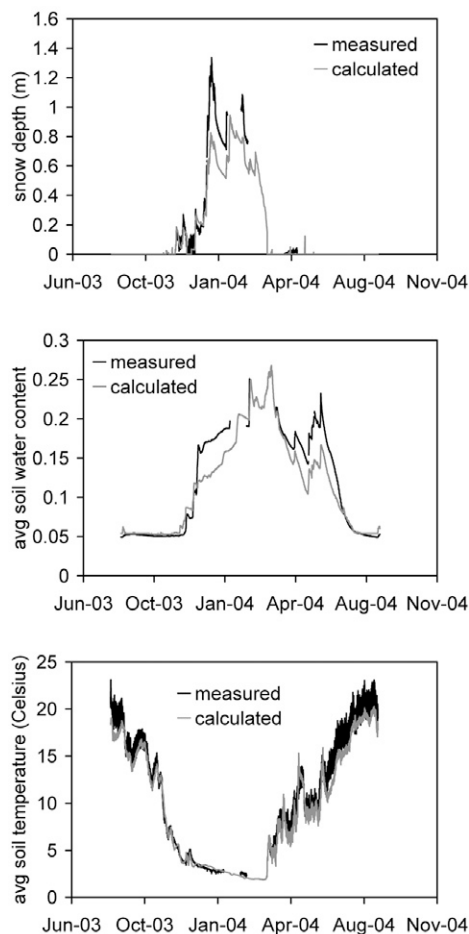


Fig. 5. Measured and calculated snow depth, profile-average soil water content, and profile-average soil temperature for Pit 100 on the northeast-facing slope of the subcatchment for the validation period.

The measured and calculated profile-average soil water content for Pit 100 is shown in Fig. 3 (RMSE = 15%, EF = 0.88). The EF = 0.88 is excellent for the profile-average soil water content for Pit 100. The five characteristic soil moisture periods ([i] summer dry; [ii] fall wetting; [iii] winter wet—low flux; [iv] spring wet—high flux; [v] late spring drying) are clearly captured by the model (McNamara et al., 2005). The good fit between the measured and calculated values is not surprising given the fact that Pit 100 data were used to optimize the Brooks–Corey hydraulic parameters for vertical soil water flow on the northeast-facing slope by Kelleners et al. (2009). The resulting hydraulic parameters were used for all

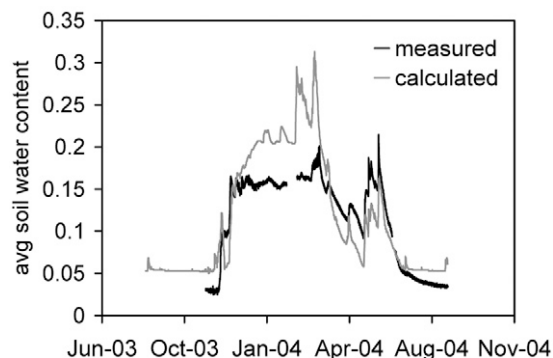


Fig. 6. Measured and calculated profile-average soil water content for time domain reflectometry transect location SU20 on the southwest-facing slope of the subcatchment for the validation period.

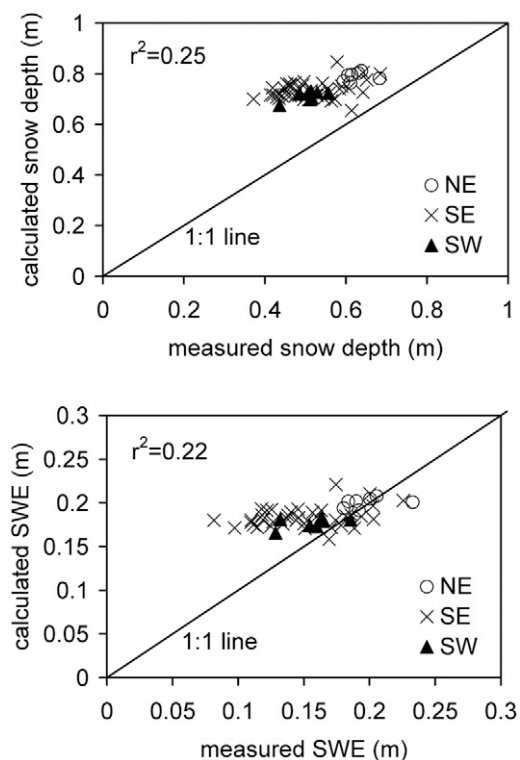


Fig. 7. Measured vs. calculated snow depth and snow water equivalent (SWE) for 57 points across the subcatchment on 10 Feb. 2004 of the validation period. Points are on the northeast-facing slope (NE), southeast-facing slope (SE), and southwest-facing slope (SW).

grid cells in this study. Figure 3 also shows that no significant soil water freezing occurs in Pit 100. The calculated maximum ice content θ_i for Pit 100 is $0.05 \text{ cm}^3 \text{ cm}^{-3}$ for the topsoil layer (results not shown).

The MCS optimized parameter values are $\theta_{fc} = 0.213$, $K_s = 19.7 \text{ m d}^{-1}$, and $K_{sr} = 0.0027 \text{ m d}^{-1}$, resulting in an objective function value $\Phi = 0.538$. The optimized value for θ_{fc} is well below the value for porosity, $\phi = 0.339$. This seems to confirm that lateral unsaturated soil water flow is an important mechanism for the steep slopes in the catchment, as suggested earlier. The saturated soil hydraulic conductivity for lateral soil water flow, $K_s = 19.7 \text{ m d}^{-1}$, is higher than expected. For comparison, the value of the saturated hydraulic conductivity for vertical soil water flow that was used is 0.3867 m d^{-1} . The resulting anisotropy factor of 51 seems unrealistic for the relatively coarse and relatively homogeneous soils in the catchment. The high optimized value for K_s may reflect the influence of soil macropores and bedrock flow paths, which result in non-Darcian preferential flow when activated under wet conditions. The optimized value for $K_{sr} = 0.0027 \text{ m d}^{-1}$ is difficult to judge because its value depends on the choice for the saturated thickness of the bedrock, D , which was assumed to be 0.2 m in this study. Using only streamflow data in the MCS parameter optimization did not significantly alter the optimized values for θ_{fc} , K_s , and K_{sr} (results not shown).

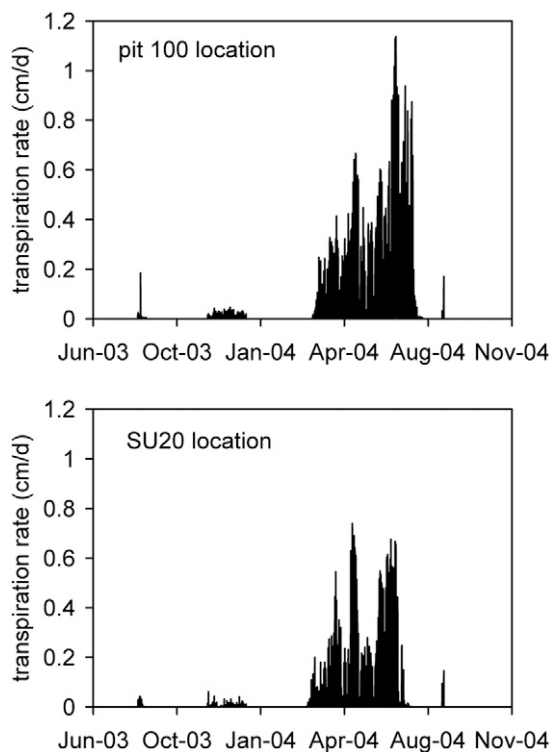


Fig. 8. Calculated transpiration rates for the Pit 100 and SU20 locations for the validation period. Values are averages across a grid cell.

The calculated water balance for the calibration period is summarized in Table 1. The calculated streamflow of 64 mm constitutes only 11% of the total incoming precipitation into the catchment of 590 mm (rain and snow). For comparison, the measured streamflow for the calibration period was 80 mm, or about 14% of the total incoming precipitation. The model results for the calibration period suggest that more water leaves the catchment through deep percolation into the bedrock than through streamflow (215 vs. 64 mm, respectively). Evapotranspiration is the most effective process for removing water from the catchment (311 mm, or 53% of total incoming precipitation). The water balance results generally agree with the results of Aishlin and McNamara (unpublished data, 2009), who used a Cl^- mass balance approach to show that from 2004 to 2008, 49% of precipitation in the subcatchment went to deep percolation and 11% to streamflow.

Model Validation Results

Measured and calculated streamflow for the validation period is shown in Fig. 4 (RMSE = 140%, EF = 0.48). Small measured streamflow events in January were not captured by the model. The timing of the main runoff between mid-February and early April was described reasonably well. The modeled flow was 1 d late and ceased 5 d too early. The total amount of streamflow was underestimated. The total measured streamflow for the validation period was 242 mm, while the total calculated streamflow was only 113 mm (see the calculated validation period water balance in Table 1). Compared with the calibration period, the RMSE rose (140 vs. 81%), signaling more error. Surprisingly, the EF also rose compared to the calibration period (0.48 vs. 0.11). The relatively high EF for the validation period does not necessarily mean that the model's ability to describe the system behavior has improved. Instead, the high EF seems to reflect the relatively high variance for the streamflow data during validation ($921 \text{ vs. } 77 \text{ L}^2 \text{ min}^{-2}$ for the calibration period). This high variance reduces the impact of model discrepancies on the EF statistic.

The measured and calculated snow depth, profile-average soil water content, and profile-average soil temperature for Pit 100 on the northeast-facing slope of the subcatchment are shown in Fig. 5. Note that the snow sensor is installed close to Pit 100 (see Fig. 1). These validation results show that the temporal dynamics in snow depth (RMSE = 52%, EF = 0.84), soil water content (RMSE = 22%, EF = 0.83), and soil temperature (RMSE = 10%, EF = 0.96) were captured well by the model. Gaps in the data are due to equipment failure. The snow pack had completely melted by the time the equipment was back online in April. The soil temperature data show that no significant soil water freezing occurs during winter. This is due to the insulating properties of the overlying snow pack.

Figure 6 shows the measured and calculated profile-average soil water content for TDR transect location SU20 on the southwest-facing slope of the subcatchment. Clearly, the performance of the model for SU20 is less satisfactory (RMSE = 37%, EF = 0.35) than for Pit 100. Systematic discrepancies of ~ 0.025 and $\sim 0.05 \text{ cm}^3 \text{ cm}^{-3}$ are

observed between the measured and calculated soil water contents for dry soil (August) and for the winter wet period (mid-December–mid-February), respectively. These discrepancies suggest that the soil water retention function used for the entire catchment (homogeneous soil assumption) is not ideal for the SU20 location. Paradoxically, the soil water retention parameters used for the catchment were determined from a multistep outflow experiment on an undisturbed soil sample taken near SU20 on the southwest-facing slope (Kelleners et al., 2009). The apparent overestimation of the initial soil water contents for SU20 is due to the fact that we initialized the model not by using measured data but by running the model twice, using the final water contents of the first run to describe the initial values for the second run.

A comparison between the measured and calculated snow depth and SWE for 57 points across the subcatchment on 10 Feb. 2004 is shown in Fig. 7. A distinction is made between points on northeast-facing slopes, southeast-facing slopes, and southwest-facing slopes. There are no northwest-facing slopes in the catchment. Calculated snow depths are all too high (top panel, $r^2 = 0.25$ for all 57 points). Most calculated SWEs are also too high (bottom panel, $r^2 = 0.22$). The differences between measured and calculated snow depth and SWE values are smallest for the northeast-facing slope.

Unfortunately, the automatic snow sensor on the northeast-facing slope was not functional on 10 February. The snow sensor data that are available for other dates show that measured snow depths are generally higher than calculated snow depths (Fig. 5). These contradictory results for the seven northeast points vs. the automatic sensor location are difficult to reconcile. It may be that blowing snow settles around the snow sensor location while most of the subcatchment, including most of the northeast-facing slope, loses snow due to wind action. The effects of blowing snow on the spatial snow distribution are not incorporated in the current model. Note that no snow physical parameters were calibrated in this study. Instead, default values were used based on detailed snow physical work by others in regions different from ours (for details, see Kelleners et al., 2009).

The calculated water balance for the validation period is different from the water balance of the calibration period (Table 1). Higher rainfall of 716 mm during the validation period led to more evapotranspiration (357 vs. 311 mm), more deep percolation (240 vs. 215 mm), and more streamflow (113 vs. 64 mm). Calculated streamflow as a percentage of the total precipitation for the validation period is 16%, compared with 11% for the calibration period. Measured streamflow as a percentage of total precipitation is 14 and 34% for the calibration and validation periods, respectively. Aishlin and McNamara (unpublished data, 2009) showed that the proportion of annual precipitation that goes to deep percolation decreases in wet years and in years with rapid snowmelt. The model results show the same pattern, with 36% of annual precipitation going to deep percolation during the calibration year and

34% going to deep percolation in the wetter validation year. The large discrepancy between measured and calculated streamflow for the validation period indicates that the model may need further improvement to accurately calculate the total amount of streamflow from the subcatchment.

Discussion

The role of vegetation in the overall water balance of the subcatchment and in the generation of runoff has received little attention in this study due to a lack of vegetation-specific data to check the model calculations. Both transpiration from dry leaf areas (root water uptake) and evaporation from wet leaf areas (intercepted water) are calculated by the model using state-of-the-art algorithms taken mainly from Oleson et al. (2004) and discussed in detail in Kelleners et al. (2009). The calculation of the temporal dynamics in LAI using Eq. [16] and the assumption of uniform root water uptake throughout the entire soil profile are admittedly simplistic and may be improved in the future. As an example, Fig. 8 shows the calculated transpiration rates $T = SC_e Q_{td} / \rho_w \gamma_v$ for the Pit 100 and SU20 locations for the validation period (SC_e is the effective soil cover, Q_{td} the latent heat flux for dry leaf surfaces, ρ_w the density of liquid water, and γ_v the latent heat of vaporization). The higher transpiration rates for Pit 100 are due to the higher soil cover ($SC_m = 0.55$) and deeper soil (1.25 m) at this location than the SU20 location ($SC_m = 0.3$, soil depth = 0.64 m). Total annual transpiration was 123 mm for Pit 100 and 70 mm for SU20. The model results suggest that plants resumed transpiration on 15 March (Pit 100) and 9 March (SU20) after most of the snow had melted.

The timing of snowmelt is critically important to model runoff generation in snowmelt-driven mountainous catchments. The melting process itself is determined by the surface energy balance. The modeling approach presented in this study was able to describe the temporal dynamics in snow accumulation, snowmelt, and soil temperature with reasonable accuracy. This provides indirect evidence that the vegetation and ground surface energy balance calculations used are realistic, at least for the northeast-facing slope (Fig. 5). No independent leaf or surface temperature measurements are available for the subcatchment to test the surface energy balance calculations directly. Distributed surface temperature measurements as well as automated measurements of snow depth and soil temperature at different locations in the subcatchment (not just on the northeast-facing slope), would facilitate a more thorough testing of this part of the model. Incorporation of a blowing snow algorithm (e.g., Essery et al., 1999; Lehning et al., 2006) may further increase the predictive capabilities of the model.

The accuracy of the soil water content calculations differs for the northeast-facing slope (Pit 100) and the southwest-facing slope (SU20). This is attributed mainly to spatial variability in soil texture. It is unrealistic to expect that one set of soil physical parameters can accurately describe all soils in the subcatchment, despite the fact that

the soil textural differences are relatively small. Direct measurement of grid-cell-specific and soil-layer-specific soil hydraulic properties is not practically feasible. Alternatively, soil hydraulic parameters may be estimated using pedotransfer functions (e.g., Gribb et al., 2009). This still leaves the effect of subgrid spatial variability, however, which is likely to be significant in complex terrain. Determination of the statistical distributions of the hydraulic parameters of the catchment soils may be more advantageous going forward. Such parameter distributions cannot be used to predict the exact soil hydraulic properties at any given point in the landscape; however, the distributions can be used to assess the influence of soil spatial variability on the calculated streamflow (e.g., Feyen et al., 2007). A limitation of applying this type of stochastic technique is the large computational burden.

The amount of streamflow is strongly influenced by the partitioning between deep percolation into the bedrock and lateral subsurface flow across the soil–bedrock interface. Lateral water flow through the weathered portion of the bedrock may also be important. The approach used in this study is admittedly simple. Our model may benefit from the addition of a groundwater reservoir in the bedrock that drains part of its water to the stream in the subcatchment, effectively adding a base flow component. A more rigorous approach would solve the soil and bedrock water flow in all three dimensions using a three-dimensional finite element model (e.g., Ebel et al., 2008). This, however, is computationally expensive. Also, the lack of information on the spatial variability in soil depth, subsurface preferential flow paths, and bedrock fracturing may not justify such a detailed approach. The modeling approach as presented in this study can be implemented in a geographic information system to ease the preparation of the model input data (e.g., Frankenberger et al., 1999).

Conclusions

The distributed model presented in this study was able to capture the temporal dynamics in snowpack, soil water content, soil temperature, and streamflow for a small mountainous catchment. Soil water content predictions for individual points in the landscape may be improved by relaxing the assumption of homogeneous soils in the model. The amount of total yearly streamflow was underpredicted by the model by 20% for the calibration period and by 53% for the validation period. This underestimation may be mitigated by including a bedrock groundwater reservoir in the model that delivers water to the stream. In the present model, all deep percolation into the bedrock is removed from the system. Adjustments in the partitioning of deep percolation into the bedrock and lateral subsurface flow toward the stream may also improve the calculated streamflow.

The model calculations suggest that 50 to 53% of the yearly incoming precipitation in the subcatchment is consumed by evapotranspiration. The model results further suggest that 34 to 36% of the incoming precipitation is transformed into deep percolation into the bedrock, while only 11 to 16% is transformed into streamflow. The true partitioning between deep percolation and streamflow is

difficult to determine. This partitioning is determined by conditions at the soil–bedrock interface, which may vary across the catchment. The main strength of the model presented in this study is the description of the temporal dynamics of the system. The quality of the streamflow predictions can be improved by refining the model physics for lateral subsurface flow and by incorporating the model into a stochastic modeling framework.

Acknowledgments

The Dry Creek Experimental Watershed is jointly operated by Boise State University and the USDA Northwest Watershed Research Center. Instrumentation was supported by NSF Grant EPS-0447689, NASA Grant NAG5-7537, and USDA-NRI Grant 2001-35102-11031. This study was funded in part by USDA-CSREES SRGP Award 2005-34552-15828.

References

- Anderson, E.A. 1976. A point energy and mass balance model of a snow cover. Tech. Rep. NWS 19. Office of Hydrol., Natl. Weather Serv., Silver Spring, MD.
- Beven, K. 1981. Kinematic subsurface stormflow. *Water Resour. Res.* 17:1419–1424.
- Beven, K.J. 1989. Changing ideas in hydrology: The case of physically-based models. *J. Hydrol.* 105:157–172.
- Bonan, G.B. 1996. A land surface model (LSM version 1.0) for ecological, hydrological, and atmospheric studies: Technical description and user's guide. Tech. Note NCAR/TN-417+STR. Natl. Ctr. for Atmos. Res., Boulder, CO.
- Brooks, R.H., and A.T. Corey. 1964. Hydraulic properties of porous media. *Hydrol. Pap.* 3. Colorado State Univ., Ft. Collins.
- Buttle, J.M., P.J. Dillon, and G.R. Eerkes. 2004. Hydrologic coupling of slopes, riparian zones and streams: An example from the Canadian Shield. *J. Hydrol.* 287:161–177.
- Chandler, D.G., M. Seyfried, M. Murdock, and J.P. McNamara. 2004. Field calibration of water content reflectometers. *Soil Sci. Soc. Am. J.* 68:1501–1507.
- Clausnitzer, V., and J.W. Hopmans. 1995. Non-linear parameter optimization: LM_OPT. General-purpose optimization code based on the Levenberg–Marquardt algorithm. *Land, Air, and Water Resour. Pap.* 100032. Univ. of California, Davis.
- Dai, Y., and Q. Zeng. 1997. A land surface model (IAP94) for climate studies: 1. Formulation and validation in off-line experiments. *Adv. Atmos. Sci.* 14:433–460.
- Dickinson, R.E., A. Henderson-Sellers, and P.J. Kennedy. 1993. Biosphere–atmosphere transfer scheme (BATS) version 1e as coupled to the NCAR community climate model. Tech. Note NCAR/TN-387+STR. Natl. Ctr. for Atmos. Res., Boulder, CO.
- Dingman, S.L. 2002. *Physical hydrology*. 2nd ed. Prentice Hall, Englewood Cliffs, NJ.
- Downer, C.W., and F.L. Ogden. 2004. GSSHA: Model to simulate diverse stream flow producing processes. *J. Hydrol. Eng.* 9:161–174.
- Dozier, J., and S.I. Outcalt. 1979. An approach toward energy balance simulation over rugged terrain. *Geogr. Anal.* 11:65–85.
- Ebel, B.A., K. Loague, D.R. Montgomery, and W.E. Dietrich. 2008. Physics-based continuous simulation of long-term near-surface hydrologic response for the Coos Bay experimental catchment. *Water Resour. Res.* 44:W07417, doi:10.1029/2007WR006442.
- Essery, R., L. Li, and J. Pomeroy. 1999. A distributed model of blowing snow over complex terrain. *Hydrol. Processes* 13:2423–2438.
- Fernandez, J.E., C. Slawinski, F. Moreno, R.T. Walczak, and M. Vanclooster. 2002. Simulating the fate of water in a soil–crop system of a semi-arid Mediterranean area with the WAVE 2.1 and the EURO-ACCESS-II models. *Agric. Water Manage.* 56:113–129.
- Feyen, L., J.A. Vrugt, B. O'Nuallain, J. van der Knijff, and A. De Roo. 2007. Parameter optimisation and uncertainty assessment for large-scale streamflow simulation with the LISFLOOD model. *J. Hydrol.* 332:276–289.
- Frankenberger, J.R., E.S. Brooks, M.T. Walter, M.F. Walter, and T.S. Steenhuis. 1999. A GIS-based variable source area hydrology model. *Hydrol. Processes* 13:805–822.
- Gribb, M.M., I. Forkutsa, A. Hansen, D.G. Chandler, and J.P. McNamara. 2009. The effect of various soil hydraulic property estimates on soil moisture simulations. *Vadose Zone J.* 8:321–331.
- Hillel, D. 2004. *Introduction to environmental soil physics*. Academic Press, San Diego.
- Huyer, W., and A. Neumaier. 1999. Global optimization by multilevel coordinate search. *J. Global Optim.* 14:331–355.
- Ivanov, V.Y., E.R. Vivoni, R.L. Bras, and D. Entekhabi. 2004. Catchment hydrologic response with a fully distributed triangulated irregular network model. *Water Resour. Res.* 40:W11102, doi:10.1029/2004WR003218.
- Jordan, R. 1991. A one-dimensional temperature model for a snow cover: Technical documentation for SNTHERM.89. Spec. Rep. 91-16. U.S. Army Corps of Eng., Cold Regions Res. and Eng. Lab., Hanover, NH.
- Kampf, S.K., and S.J. Burges. 2007. A framework for classifying and comparing distributed hillslope and catchment hydrologic models. *Water Resour. Res.* 43:W05423, doi:10.1029/2006WR005370.
- Kavvas, M.L., Z.Q. Chen, C. Dogrul, J.Y. Yoon, N. Ohara, L. Liang, H. Aksoy, M.L. Anderson, J. Yoshitani, K. Fukami, and T. Matsuura. 2004. Watershed environmental hydrology (WEHY) model based on upscaled conservation equations: Hydrologic module. *J. Hydrol. Eng.* 9:450–464.
- Kavvas, M.L., Z.Q. Chen, L. Tan, S.T. Soong, A. Terakawa, J. Yoshitani, and K. Fukami. 1998. A regional-scale land surface parameterization based on areally-averaged hydrological conservation equations. *Hydrol. Sci. J.* 43:611–631.
- Kelleners, T.J., D.G. Chandler, J.P. McNamara, M.M. Gribb, and M.S. Seyfried. 2009. Modeling the water and energy balance of vegetated areas with snow accumulation. *Vadose Zone J.* 8:1013–1030.
- Lehning, M., I. Volksch, D. Gustafsson, T.A. Nguyen, M. Stahli, and M. Zappa. 2006. ALPINE3D: A detailed model of mountain surface processes and its application to snow hydrology. *Hydrol. Processes* 20:2111–2128.
- Loague, K., and R.E. Green. 1991. Statistical and graphical methods for evaluating solute transport models: Overview and application. *J. Contam. Hydrol.* 7:51–73.
- Marks, D., and J. Dozier. 1979. A clear-sky longwave radiation model for remote alpine areas. *Arch. Meteorol. Geophys. Bioklimatol., Ser. B* 27:159–187.
- McNamara, J.P., D. Chandler, M. Seyfried, and S. Achet. 2005. Soil moisture states, lateral flow, and streamflow generation in a semi-arid, snowmelt-driven catchment. *Hydrol. Processes* 19:4023–4038.
- Miller, C.R., P.S. Routh, T.R. Brosten, and J.P. McNamara. 2008. Application of time-lapse ERT imaging to watershed characterization. *Geophysics* 73:G7, doi:10.1190/1.2907156.
- Muneer, T. 1997. *Solar radiation and daylight models for energy efficient design of buildings*. Architectural Press, Oxford, UK.
- Oleson, K.W., Y. Dai, G. Bonan, M. Bosilovich, P. Dirmeyer, F. Hoffman, et al. 2004. Technical description of the Community Land Model (CLM). Tech. Note NCAR/TN-461+STR. Natl. Ctr. for Atmos. Res., Boulder, CO.
- Press, W.H., S.A. Teukolsky, W.T. Vetterling, and B.P. Flannery. 1992. *Numerical recipes in FORTRAN*. 2nd ed. Cambridge Univ. Press, Cambridge, UK.
- Robinson, D.A., C.S. Campbell, J.W. Hopmans, B.K. Hornbuckle, S.B. Jones, R. Knight, F. Ogden, J. Selker, and O. Wendroth. 2008. Soil moisture measurement for ecological and hydrological watershed-scale observatories: A review. *Vadose Zone J.* 7:358–389.
- Ross, P.J. 2003. Modeling soil water and solute transport: Fast, simplified numerical solutions. *Agron. J.* 95:1352–1361.
- Seyfried, M.S., L.E. Grant, D. Marks, A. Winstral, and J. McNamara. 2009. Simulated soil water storage effects on streamflow generation in a mountainous snowmelt environment, Idaho, USA. *Hydrol. Processes* 23:858–873.
- Singh, V.P., and D.K. Frevert (ed.). 2002. *Mathematical models of small watershed hydrology and applications*. Water Resour. Publ., Highlands Ranch, CO.
- Slagstad, T., K. Midttome, R.K. Ramstad, and D. Slagstad. 2008. Factors influencing shallow (<1000 m depth) temperatures and their significance for extraction of ground-source heat. p. 99–109. *In* T. Skagstad (ed.) *Geology for society*. Spec. Publ. 11. Geol. Surv. of Norway, Trondheim.
- Topp, G.C., J.L. Davis, and A.P. Annan. 1980. Electromagnetic determination of soil water content: Measurements in coaxial transmission lines. *Water Resour. Res.* 16:574–582.
- Tromp-van Meerveld, H.J., and J.J. McDonnell. 2006. Threshold relations in subsurface stormflow: 2. The fill and spill hypothesis. *Water Resour. Res.* 42:W02411, doi:10.1029/2004WR003800.
- Vanclooster, M., J.J.T.I. Boesten, M. Trevisan, C.D. Brown, E. Capri, O.M. Eklo, B. Gottesburen, V. Gouy, and A.M.A. van der Linden. 2000. A European test of pesticide-leaching models: Methodology and major recommendations. *Agric. Water Manage.* 44:1–19.
- Vrugt, J.A., H.V. Gupta, L.A. Bastidas, W. Bouten, and S. Sorooshian. 2003. Effective and efficient algorithm for multiobjective optimization of hydrologic models. *Water Resour. Res.* 39:1214, doi:10.1029/2002WR001746.
- Wigmosta, M.S., B. Nijssen, and P. Storck. 2002. The distributed hydrology soil vegetation model. p. 7–42. *In* V.P. Singh and D.K. Frevert (ed.) *Mathematical models of small watershed hydrology and applications*. Water Resour. Publ., Highlands Ranch, CO.
- Wigmosta, M.S., L.W. Vail, and D.P. Lettenmaier. 1994. A distributed hydrology–vegetation model for complex terrain. *Water Resour. Res.* 30:1665–1679.
- Williams, C.J. 2005. Characterization of the spatial and temporal controls on soil moisture and streamflow generation in a semi-arid headwater catchment, Dry Creek Experimental Watershed, Boise, Idaho. M.S. thesis. Boise State Univ., Boise, ID.
- Zhang, W., and D.R. Montgomery. 1994. Digital elevation model grid size, landscape representation, and hydrologic simulations. *Water Resour. Res.* 30:1019–1028.